



Expansion Properties of the Young Supernova Type Iax Remnant Pa 30 Revealed

Tim Cunningham^{1,12} , Ilaria Caiazzo^{2,3} , Nikolaus Z. Prusinski⁴ , James Fuller³ , John C. Raymond¹ , S. R. Kulkarni³ , James D. Neill³ , Paul Duffell⁵ , Chris Martin³ , Odette Toloza^{6,7} , David Charbonneau¹ , Scott J. Kenyon¹ , Zeren Lin³, Mateusz Matuszewski³ , Rosalie McGurk⁸ , Abigail Polin^{5,9,10} , and Philippe Z. Yao¹¹

¹ Center for Astrophysics—Harvard & Smithsonian, 60 Garden St., Cambridge, MA 02138, USA; tim.cunningham@cfa.harvard.edu

² Institute of Science and Technology Austria, Am Campus 1, 3400 Klosterneuburg, Austria

³ Division of Physics, Mathematics and Astronomy, California Institute of Technology, Pasadena, CA 91125, USA

⁴ Cahill Center for Astronomy and Astrophysics, California Institute of Technology, 1200 E. California Blvd. MC 249-17, Pasadena, CA 91125, USA

⁵ Department of Physics and Astronomy, Purdue University, 525 Northwestern Ave., West Lafayette, IN 47907, USA

⁶ Departamento de Física, Universidad Técnica Federico Santa María, Av. España 1680, Valparaíso, Chile

⁷ Millennium Nucleus for Planet Formation, NPF, Valparaíso, Av. España 1680, Chile

⁸ W. M. Keck Observatory, Kamuela, HI, USA

⁹ The Observatories of the Carnegie Institution for Science, 813 Santa Barbara St., Pasadena, CA 91101, USA

¹⁰ TAPIR, Walter Burke Institute for Theoretical Physics, 350-17, Caltech, Pasadena, CA 91125, USA

¹¹ Department of Astrophysical Sciences, Princeton University, Peyton Hall, Princeton, NJ 08544, USA

Received 2024 June 11; revised 2024 August 19; accepted 2024 August 19; published 2024 October 24

Abstract

The recently discovered Pa 30 nebula, the putative type Iax supernova remnant associated with the historical supernova of 1181 AD, shows puzzling characteristics that make it unique among known supernova remnants. In particular, Pa 30 exhibits a complex morphology, with a unique radial and filamentary structure, and it hosts a hot stellar remnant at its center, which displays oxygen-dominated, ultrafast winds. Because of the surviving stellar remnant and the lack of hydrogen and helium in its filaments, it has been suggested that Pa 30 is the product of a failed thermonuclear explosion in a near- or super-Chandrasekhar white dwarf, which created a subluminescent transient, a rare subtype of the Ia class of supernovae called type Iax. We present here a detailed study of the 3D structure and velocities of a full radial section of the remnant. The Integral Field Unit observations, obtained with the new red channel of the Keck Cosmic Web Imager spectrograph, reveal that the ejecta are consistent with being ballistic, with velocities close to the free-expansion velocity. Additionally, we detect a large cavity inside the supernova remnant and a sharp inner edge to the filamentary structure, which coincides with the outer edge of a bright ring detected in infrared images. Finally, we detect a strong asymmetry in the amount of ejecta along the line of sight, which might hint at an asymmetric explosion. Our analysis provides strong confirmation that the explosion originated from SN 1181.

Unified Astronomy Thesaurus concepts: Type Ia supernovae (1728); Supernova remnants (1667); Emission nebulae (461); Spectroscopy (1558)

1. Introduction

The “Guest Star” recorded in 1181 AD by Chinese and Japanese astronomers is one of only five confirmed Galactic supernovae (SNe) recorded in human history. Until recently, SN 1181 was the youngest Galactic supernova without an associated remnant identified with confidence. In 2013, the nebula Pa 30 was discovered by amateur astronomer Dana Patchick in the Wide-field Infrared Survey Explorer (WISE; E. L. Wright et al. 2010) archive (Cutri et al. 2012; Q. A. Parker et al. 2016) and there is mounting evidence, including its age and sky location, that this nebula is the supernova remnant associated with SN 1181 (A. Ritter et al. 2021; B. E. Schaefer 2023).

Pa 30 is a unique SN remnant for several reasons. A hot star (IRAS 00500+6713, 2MASS J00531123+6730023), with a surface temperature of about 200,000 K, is at its center and shows strong outflows with extreme velocities in excess of

15,000 km s^{−1} (V. V. Gvaramadze et al. 2019; F. Lykou et al. 2023). Both spectra of the central star and of the nebula lack any indication of hydrogen or helium, while an X-ray spectrum of the nebula reveals carbon-burning ashes (L. M. Oskinova et al. 2020). Also, the morphology of the SN remnant, revealed by narrowband images in [S II] (R. A. Fesen et al. 2023, see Figure 1), has a structure never seen before in an SN remnant, with narrow, almost radial filaments distributed in a spherically symmetric fashion around the central star.

Because of the presence of a surviving stellar remnant and the composition of the star’s wind and of the nebula, it has been suggested that Pa 30 is the product of a thermonuclear runaway reaction in a near- or super-Chandrasekhar white dwarf that failed to produce a detonation or failed to explode the entire star, producing a subluminescent transient (V. V. Gvaramadze et al. 2019; L. M. Oskinova et al. 2020; A. Ritter et al. 2021; F. Lykou et al. 2023; R. A. Fesen et al. 2023). This type of transient has been associated with the subclass of type Ia supernovae called type Iax. Type Iax supernovae also show lower expansion velocities near maximum than normal type Ia, which is consistent with the low velocities detected in Pa 30 (R. J. Foley et al. 2013). It has been suggested that the Iax supernova was caused by a double-degenerate white dwarf merger (V. V. Gvaramadze et al. 2019; P. Z. Yao et al. 2023),

¹² NASA Hubble Fellow.



Original content from this work may be used under the terms of the [Creative Commons Attribution 4.0 licence](https://creativecommons.org/licenses/by/4.0/). Any further distribution of this work must maintain attribution to the author(s) and the title of the work, journal citation and DOI.

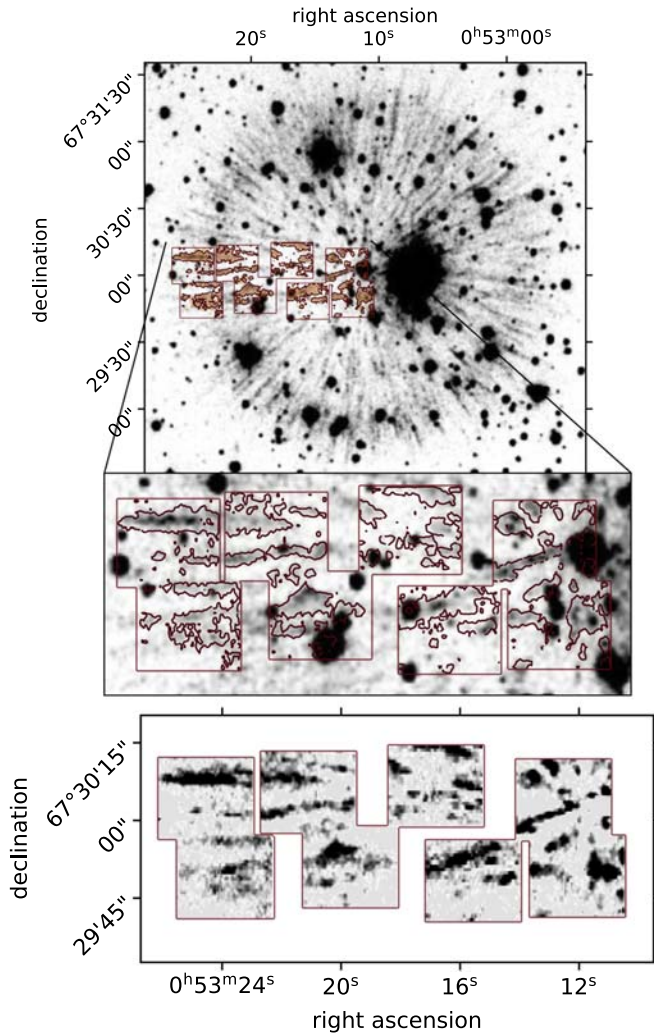


Figure 1. Lower panel: narrowband image obtained from stacking all the KCWI-red channel cubes and integrating over the wavelength range 6680–6750 Å, covering the maximally blue- and redshifted [S II] emission features. Upper panel: the black and white image shows the [S II] narrowband data from R. A. Fesen et al. (2023), obtained with the Hiltner telescope at Kitt Peak. Superimposed in orange and with a large transparency, we show for comparison the same KCWI-red image as in the lower panel. The zoomed-in panel shows in red the contours of the filaments in the KCWI-red image: the same filaments are detected in the two images, but the KCWI-red image is deeper, allowing the detection of fainter features.

and that the high-speed winds on the surface of the remnant are magnetically driven (V. V. Gvaramadze et al. 2019; Y. Zhong et al. 2024).

The morphology of the nebula is strikingly different from the clumpy internal structures typically observed in type Ia remnants, which are caused by a combination of Rayleigh–Taylor instability (RTI) and Kelvin–Helmholtz instability (KHI). On the other hand, examples of somewhat radial filamentary structures have been observed in the wind-blown tails of novae, like GK Persei and DQ Herculis (N. M. H. Vaytet et al. 2007; M. M. Shara et al. 2012), and as cometary tails in the infrared images of some planetary nebulae (C. R. O’Dell & K. D. Handron 1996; R. Wesson et al. 2024). In analogy to these systems, R. A. Fesen et al. (2023) suggested that the unusual filamentary structure in Pa 30 is connected to the high-velocity wind of the central star, that is accelerating parts of the clumpy, low-density ejecta, and

morphing them into filaments by the effect of RTI (see also T. Ko et al. 2024).

However, in the above examples, it is always possible to identify a clump undergoing visible mass loss, while there is no obvious density variation or clumps in Pa 30’s filaments. Also, the wind-driven scenario does not explain why the turbulence generated by KHI does not destroy the filaments. In an alternative model, P. C. Duffell et al. (2024) proposed that the filaments are created by RTI in the interaction between the SN ejecta and the circumstellar medium (CSM), and that the KHI in the filaments is suppressed via efficient line cooling. They were able to reproduce the radial structure of the filaments in Pa 30, and made a few predictions on what could be observed in the remnant. In particular, they found the velocity structure in the filaments to be nearly ballistic.

The peculiarity of Pa 30’s morphology is also revealed in the infrared and in X-rays. The WISE image in the W4 filter centered at 22 μm shows a diffuse infrared halo with an angular size of about 100'' in radius, and a smaller, brighter ring extending to about an arcminute (V. V. Gvaramadze et al. 2019; R. A. Fesen et al. 2023). V. V. Gvaramadze et al. (2019) suggested that the infrared nebular emission could be dominated by [O IV] 25.89 μm and [Ne V] 14.32 and 24.32 μm lines. On the other hand, photoionization modeling performed by P. Z. Yao et al. (2023) shows that if the progenitor of the Pa 30 remnant is a double C/O white dwarf merger, the measured fluxes in the WISE filters W3 (12 μm) and W4 (22 μm) are likely to be dominated by dust emission, rather than line emission (see their Figure 8). F. Lykou et al. (2023) also performed photoionization modeling of the infrared spectral energy distribution (SED) of the nebula out to longer IR wavelengths covering the 12–160 μm range, as measured by WISE, IRAS, and AKARI (see their Figure 12). Their results suggested that the emission at shorter wavelengths ($\lesssim 30 \mu\text{m}$) is likely dominated by strong emission lines of [Ne VI], [Ne V], and [O IV] at 7.6, 14.7, and 25.9 μm , respectively, as proposed by V. V. Gvaramadze et al. (2019), while the SED at longer wavelengths cannot be explained by emission lines but is consistent with emission from dust. JWST spectroscopy and narrowband imaging would help reveal the origin of the infrared emission in this peculiar source.

In X-rays, the system has been imaged using XMM-Newton (F. Jansen et al. 2001) and the Chandra X-ray Observatory (M. C. Weisskopf et al. 2000). An outer nebula is detected with XMM to have an angular size comparable to that of the halo, while a much smaller inner nebula is detected as a point source in XMM and it is resolved to be about 1''.5 in Chandra (L. M. Oskinova et al. 2020; T. Ko et al. 2024). While the edge of the outer X-ray nebula might correspond to the location of the forward shock, where the ejecta is interacting with the unperturbed CSM, the origin of the inner nebula is more uncertain (P. C. Duffell et al. 2024). It has been suggested that the inner X-ray nebula corresponds to the location of the wind termination shock, where the high-speed winds from the white dwarf run into the much slower ejecta from the supernova (T. Ko et al. 2024).

We here report Integral Field Unit (IFU) spectroscopic observations of the Pa 30 nebula that reveal a rich morphology in the SN ejecta and provide the first 3D characterization of the velocity and spatial structure of the nebula. This allows the first accurate determination of the inner edge of the filaments, providing a key constraint for dynamical models of the ejecta.

In Section 2 we describe the observations, in Section 3.1 we show the sky location of the strongest emission features, in Section 3.2 we present the full velocity map, and in Sections 3.3 and 3.4 we present a deprojection of the velocities. In Section 4 we provide a summary of our findings.

2. Observations

We observed a radial section of the nebula (see Figure 1) using the blue and the new red arm of the Keck Cosmic Web Imager (KCWI; P. Morrissey et al. 2018) IFU on the Keck II Telescope on Maunakea. We used the low-dispersion gratings, BL and RL, with the medium slicer on the two arms of the IFU. This configuration yields a field of view (FOV) of $16''.5 \times 20''.4$, a spatial resolution of $0''.7$, and a spectral resolution of $R \simeq 1800$ on the blue side and of $R \simeq 1600$ on the red side. We used a detector binning of 2×2 for all our pointings. Figure 1 shows the location of our mosaic tiles superimposed on the [S II] image from R. A. Fesen et al. (2023). For each tile, we obtained a single 2000 s exposure with KCWI-blue and six separate 300 s exposures with KCWI-red. This combination leads to a similar exposure time in both the blue and red channels and mitigates the high influx of cosmic rays on the red side. For the top-right pointing, which contains the central star, we also obtained a shorter 120 s exposure to avoid saturation. We will present an analysis of our spectrum of the central star in an upcoming paper. More details on the data reduction and analysis are given in Appendix A.

3. Results

3.1. Integrated Images and Spectra

Figure 1 shows the filamentary structure revealed by integrating the stacked KCWI-red data cubes across the wavelength range 6680–6750 Å, which covers the blue- and redshifted emission from the [S II] doublet, compared to the narrowband image from R. A. Fesen et al. (2023). The top panel shows that the filaments detected with KCWI-red are coincident with some of the brightest filaments in the narrowband imaging. However, the KCWI-red data allows us to detect fainter features, which leads to a higher filling factor than implied by the narrowband image from R. A. Fesen et al. (2023). In the KCWI-red and KCWI-blue data, we also detect filaments with emission lines attributed to [O III] (at 5007 Å) and [Ar III] (at 7136 Å). This Letter focuses on the velocity structure of the nebula derived from the strongest emission features, the [S II] doublet. In a follow-up paper, we will present a detailed analysis of the full data set, including the other emission lines.

3.2. Velocity Mapping

To construct a velocity map of the nebula, we analyze the Doppler shift of the [S II] doublet in all filaments. In order to reduce contamination from noise, we focus only on the spatial regions that lie within the brightest filaments, i.e., within the contours shown in red in Figure 1. Details on the production of the mask are given in Appendix A.

At every spatial pixel included within the selected regions, we identify the [S II] doublet and perform a double-Gaussian fit to the spectrum in the range 6630–6820 Å, mean-averaged over a 3×3 pixel window centered on the given pixel location. In some pixels, we can find contributions from more than one

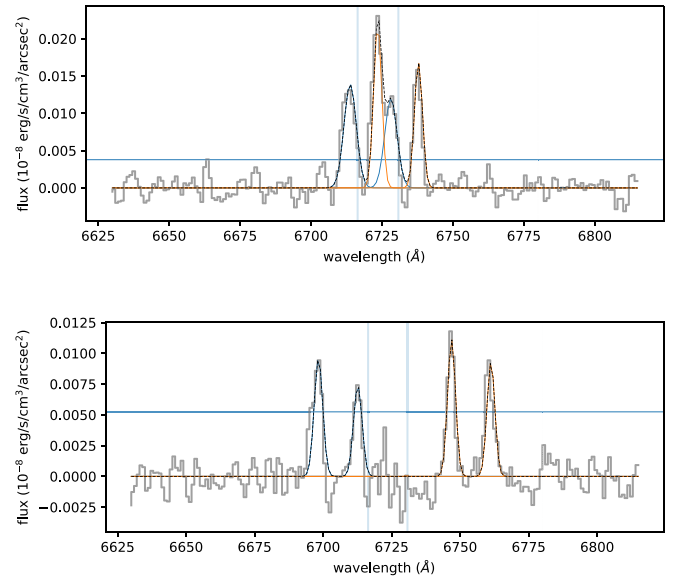


Figure 2. Examples of the Gaussian-fitting to the blue- and redshifted [S II] doublets. Each panel shows the mean-averaged spectrum over a 3×3 sky pixel region. The horizontal blue line indicates a 3σ noise threshold relative to the local continuum. The two vertical lines indicate the rest wavelengths of the [S II] 6717 Å/6731 Å doublet.

filament at different velocity shifts. For this reason, we fit additive pairs of Gaussians, either one, two, three, or four pairs, to all detected doublets with emission that peaks at least 3σ above the local continuum noise level. The two Gaussians in each pair have a fixed wavelength separation of $\Delta\lambda = 6730.78 - 6716.42 = 14.6$ Å, and the amplitude ratio is limited to the range $0.5 \leq A_{6717}/A_{6731} \leq 1.3$. The low- and high-density limits of 1.3 and 0.5 are determined purely by the atomic rates (see, for instance, Figure 9 of J. Y. Seok et al. 2020, for the ratio from the atomic database for emission lines CHIANTI; G. Del Zanna et al. 2015). Although the true low-density limit is ≈ 1.42 , densities much below 100 cm^{-3} would not produce significant observable [S II] emission, so we use a more restricted range. Figure 2 shows an example of the spectral fitting. The measured wavelength of the doublet provides the Doppler-shifted line-of-sight velocity of the filament(s). The spatial dependence of the measured velocities is shown in Figure 3.

Near the central star, we measure absolute velocities up to $\approx 1400 \text{ km s}^{-1}$, higher than the $\approx 1100 \text{ km s}^{-1}$ reported by previous single-slit spectroscopic observations (A. Ritter et al. 2021; R. A. Fesen et al. 2023). We also find strong variation in velocity along the filaments, many of which show a clear increase in velocity as a function of radius. Although some filaments are predominantly redshifted or blueshifted, many of the bright filaments appear to show contributions from both blue- and redshifted components. Such apparent spatial correlation is likely not significant, as we only observed a small fraction of the nebula. To investigate if there is an actual spatial correlation between blue- and redshifted emission, we performed two statistical tests.

In our fitting procedure, we focused on the pixels with the brightest emission. Such selection resulted in fits of 8903 unique [S II] doublet. Among those were a total of 4888 redshifted and 4015 blueshifted doublets. In total, 5575 unique pixels yielded a fit of at least one doublet, while 2894 pixels yielded a fit of two or more doublets. In short, we find that the

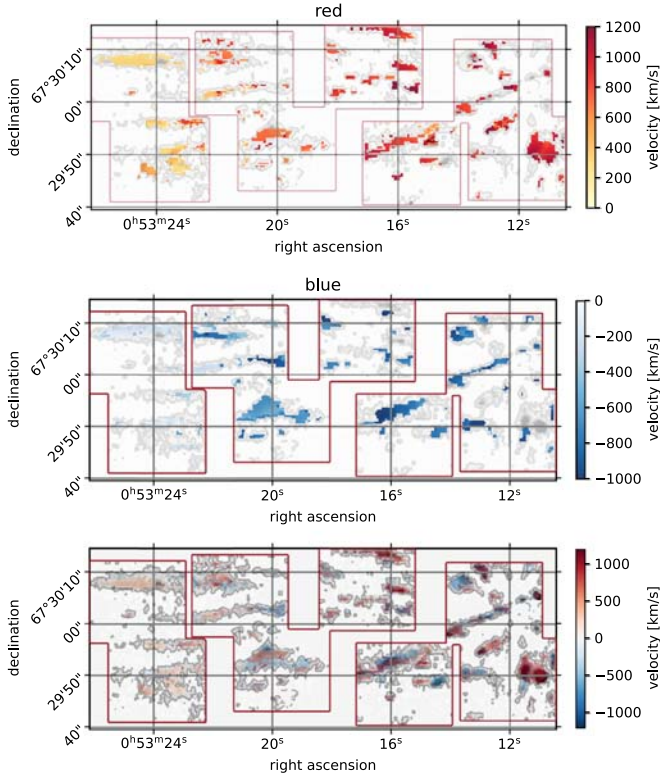


Figure 3. Upper panel: velocity map for all sky positions with detectable redshifted emission in the [S II] 6717/6731 Å doublet. We find a line-of-sight velocity gradient as a function of projected sky distance to the central star, which strongly implies a homologous velocity profile. Middle: similar to the top panel, but for all measured blueshifted components. Lower: combined velocity map for all filaments.

fraction of pixels with more than one distinct velocity contribution is $2894/5575 = 0.52$, which is not negligible but shows that any given pixel is just as likely to have one rather than multiple velocity contributions. To further test the significance of this apparent correlation we perform a 2D Kolmogorov–Smirnov (KS) test on the spatial position of two samples; one sample containing the sky coordinates of all redshifted fitted doublets, the other sample containing the coordinates of all blueshifted components. The 2D KS test is performed using the public code NDTEST,¹³ which provides a PYTHON implementation of the 2D KS test algorithm developed by J. A. Peacock (1983) and later improved by G. Fasano & A. Franceschini (1987). The p -value from the 2D KS test provides an estimate of the probability with which the null hypothesis can be ruled out. In this case, the null hypothesis that the two samples are drawn from the same spatial distribution has a probability of $p < 10^{-17}$. We thus conclude that there is likely no significant correlation between the sky position of red- and blueshifted material in these KCWI observations.

3.3. Deprojection

The measurement of the sky position and line-of-sight velocity for each filament allows, for the first time, a fully 3D reconstruction of the Pa 30 nebula. We adopt the distance to the central star to be $D = 2.3^{+0.1}_{-0.1}$ kpc, as presented in the geometric Gaia distance catalog of C. A. L. Bailer-Jones et al. (2021).

¹³ Written by Zhaozhou Li, <https://github.com/syrte/ndtest>.

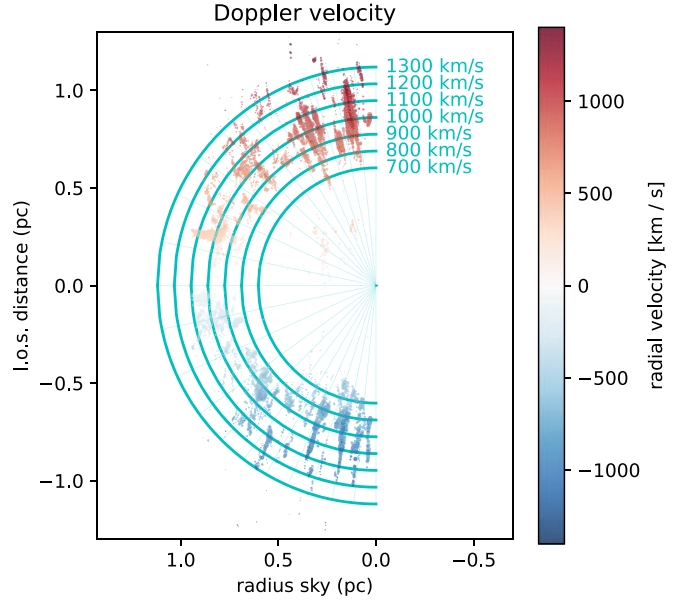


Figure 4. Deprojected radial structure of the observed fraction of the nebula assuming that all material was ejected in the year 1181 and that the velocities have remained constant in time. The x -axis shows the radial distance between the central star and a given filament projected on the plane of the sky assuming the Gaia distance to the central star of $D = 2.3$ kpc. The y -axis shows the reconstructed line-of-sight distance from the central star, using Equation (1) and an age of $\tau = 842$ yr.

First, we deproject the structure of Pa 30 by assuming that the measured ejecta velocities have been constant in time since the year 1181, and that all gas with detected emission was ejected simultaneously. Therefore, for each measured line-of-sight velocity, v_{los} , we find the line-of-sight distance from the central star as

$$d_{\text{los}} = v_{\text{los}} \tau, \quad (1)$$

where we take the age of the remnant to be $\tau = 842$ yr. In Figure 4, we plot the recovered d_{los} as well as the line-of-sight velocities. We can see that the structure in Figure 4 is very close to being spherically symmetric. After the deprojection, we can clearly see a cavity near the central star. There is still a small percentage of pixels (2.6%) redshifted side close to the central star (in the region defined by $r_{\text{sky}} < 0.5$ pc and $0.0 < d_{\text{los}} < 0.5$ pc); visual inspection of the spectra of the 229 pixels that produce doublets in that region reveals that they are mostly due to contamination from a stationary sky line, which was not properly removed for this small percentage of pixels. Because of their small fluxes, these noisy pixels do not affect our analysis.

Since the line-of-sight velocities measured by Doppler shifts indicate the current velocities in the ejecta, while the sky location of the ejecta divided by the time since the explosion carries information on how the velocities have changed since the explosion, it is not obvious that the spatial structure should appear symmetric after the deprojection. In fact, asymmetry between the x - and the y -axis in Figure 4 can be expected in three cases: (1) the assumed age for the remnant is incorrect, (2) the velocities in the nebula are not ballistic, and the ejecta has been slowed down or accelerated since the supernova, or (3) the velocity of the ejecta along the line of sight is intrinsically different to velocities in the sky plane.

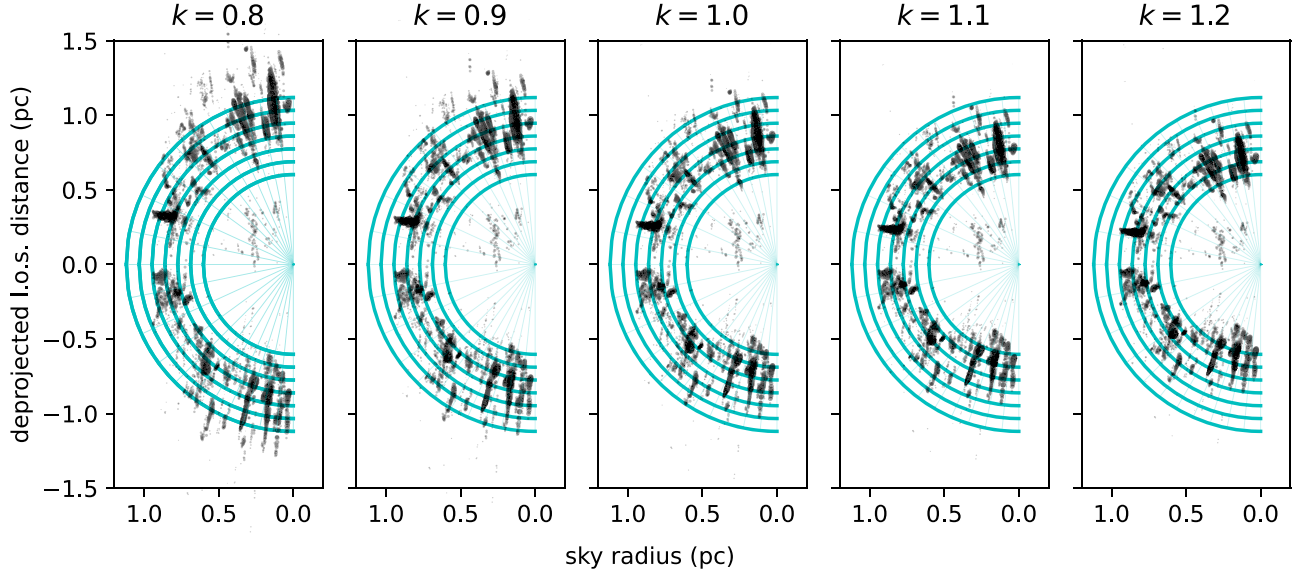


Figure 5. Deprojection of the measured line-of-sight velocities and sky position. The x -axis parameter, sky radius, describes the distance between the central star and any given point on the sky, collapsing the 2D sky positions into one dimension only. The parameter k , increasing from left to right, indicates the fraction of the ballistic velocity used in the deprojection. Under the assumptions that all material was ejected in the year 1181 and that the nebula has approximately spherical symmetry (as implied by the existing narrowband imaging; R. A. Fesen et al. 2023), we can see qualitatively that k should be close to unity, and therefore that the velocities in the ejecta are close to the ballistic free-expansion velocity. The contours show the predicted spatial location for material ejected at different velocities, from 700 km s^{-1} at the inner edge, to 1300 km s^{-1} at the outer edge.

We parameterize the amount by which the filaments deviate from fully ballistic by defining the ballistic fraction, k , such that

$$v = \frac{kr}{\tau}, \quad (2)$$

where r is the radial distance from the central star and τ is the time since the supernova explosion. From the data, we can only constrain the ratio k/τ , as the two parameters are fully degenerate.

Lifting the assumption that the ejecta is homologous, the line-of-sight distance is now given by

$$d_{\text{los}} = \frac{v_{\text{los}} \tau}{k}. \quad (3)$$

In Figure 5, we plot the line-of-sight distance converted from the measured Doppler shift by using Equation (3) against the measured sky radius, which is defined as the distance from the central star on the sky in parsec. In the different panels, we keep $\tau = 842 \text{ yr}$ and increase, from left to right, the ballistic fraction k from 0.8 to 1.2, in order to demonstrate the effects of varying the k/τ ratio. We emphasize that in reality, we are varying the k/τ ratio as the two parameters are degenerate. Qualitatively, we can see that the ejecta look approximately spherically symmetric when we assume $k \sim 1.0$.

To quantitatively constrain the ratio k/τ , in Figure 6 we perform an elliptical fit to the spatial distribution of the filaments, reconstructed using Equation (1). The data points are reflected across the plane defined by $r_{\text{sky}} = 0$ to enable an elliptical regression. Since the sky radius is by definition positive, this is equivalent to fitting the nonreflected data with a semiellipse. However, the full ellipse is computationally convenient and we do not expect this reflection to alter the statistical conclusions from this analysis. The best-fit deprojection contour (black solid line) is found using a linear least-squares Levenberg–Marquardt algorithm implemented

in the SCIPY package LEAST_SQUARES. The fit is performed over five parameters that describe the ellipse: a , b , x_0 , y_0 , and θ , which represent the semimajor axis, semiminor axis, the x - y origin, and the angle of rotation between the semimajor axis and the $x = 0$ plane. The fit is performed by minimizing the geometric distance between the data points and the ellipse. The geometric distances are weighted by the integrated intensity, I , in the two emission lines of the detected [S II] doublet (see Figure 2). The integral is described analytically by $I = \sqrt{2\pi}((\sigma A)_{6717} + (\sigma A)_{6730})$, where A and σ are the fitted Gaussian amplitude and standard deviation, respectively. The uncertainty on the fit is shown in the figure by sampling the multivariate normal distribution described by the covariance matrix from the least-squares regression. The 1000 drawn samples are plotted in orange.

From the best-fit ellipse parameters, the ratio of the semiminor and -major axes quantifies the asymmetry in the distribution, with $b/a = 1$ indicating a perfect circle. If we assume that our estimate of the age is correct, the ratio of the semiminor and -major axes can then be directly converted into an estimate of k . We find

$$k = \frac{b}{a} = 0.97^{+0.09}_{-0.08} \times \left(\frac{\tau}{842 \text{ yr}} \right) \left(\frac{D}{2297 \text{ pc}} \right)^{-1}, \quad (4)$$

where the quoted 1σ uncertainty includes the 1σ uncertainty on the fitted parameters and on the Gaia distance posterior (C. A. L. Bailer-Jones et al. 2021). On the other hand, assuming that the ejecta has not been slowed down at all by the CSM ($k \equiv 1$), nor accelerated by any mechanism, we can derive an age of the remnant, and therefore the time of explosion to be

$$t_0 = 2023 - \tau = 1152^{+77}_{-75} \text{ yr}. \quad (5)$$

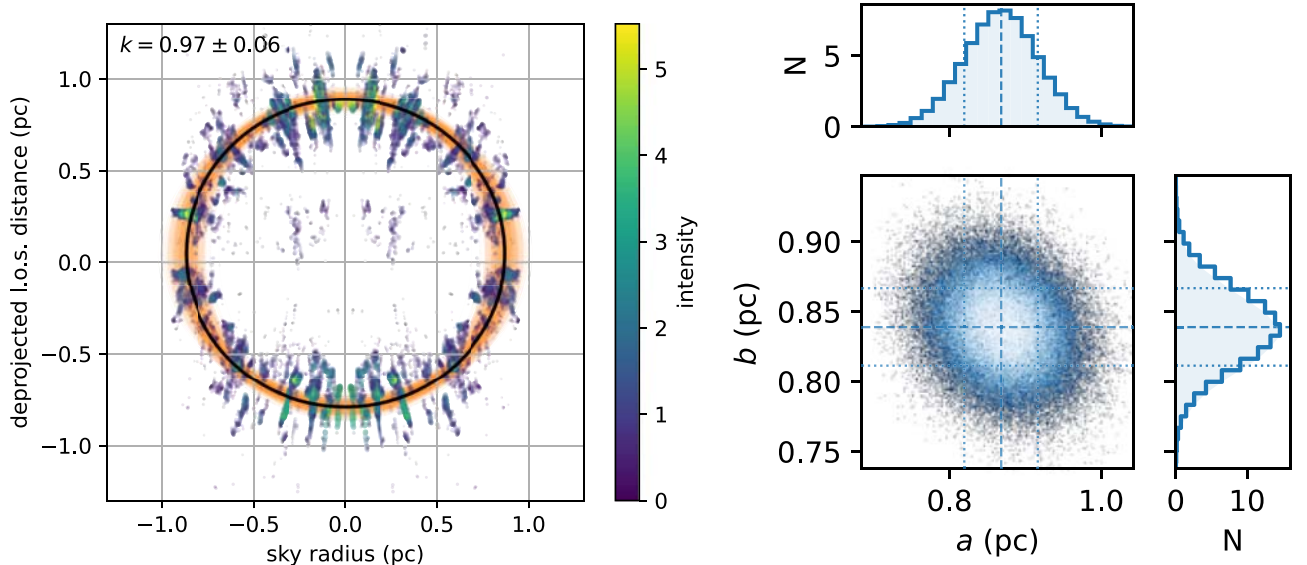


Figure 6. Deprojection fit with the assumptions outlined in the caption of Figure 5. The measured Doppler shift is converted into a line-of-sight distance using Equation (1), and plotted against the measured sky radius, which is defined as the distance from the central star on the sky in parsec. The central star is located at the origin of the graph. The data is reflected across the plane defined by $r_{\text{sky}} = 0$ to enable an elliptical regression. The best-fit deprojection contour (solid) is found using the linear least-squares Levenberg–Marquardt algorithm to fit for the five parameters of the ellipse: a , b , x_0 , y_0 , and θ , which represent the semimajor axis, semiminor axis, x - y origin, and angle. The ballistic fraction, k , is then given by $k = b/a$. This yields a best-fit value of $k = 0.97^{+0.09}_{-0.08}$, where the 1σ uncertainties also account for the uncertainty on the Gaia distance. The fitted values for the center of the ellipse are $x_0 = 0.00 \pm 0.05$ pc and $y_0 = 0.05 \pm 0.03$ pc. Right: posterior distribution of a and b from the elliptical regression shown in the left panel.

This result is consistent with the nebula being ejected in the year 1181, and provides a strong indication that the nebula is the remnant of the historic supernova.

Finding k close to unity means that the ejecta have not been accelerated or decelerated significantly since the explosion. It is expected that the ejecta should start decelerating once the forward shock has swept up a mass comparable to the ejecta mass itself, and then the deceleration should continue as more mass is swept up until the expansion enters the adiabatic or “Taylor–Sedov” phase. L. M. Oskinova et al. (2020) derived an ejecta mass of $M_{\text{ej}} \sim 0.1 M_{\odot}$ for Pa 30, based on the measured angular size and emission measure of the outer X-ray nebula, which is consistent with the expected ejecta mass from double white dwarf mergers (J. Schwab 2021). Given a radius of ≈ 1 pc, the ejecta would have swept up ~ 0.1 – $1 M_{\odot}$ given a typical interstellar medium (ISM) particle density of ~ 1 – 10 cm^{-3} ; however, the planetary nebula(e) that gave rise to the white dwarf(s) might have created a lower-density region around the system.

3.4. Velocity Distribution

In the top panel of Figure 7, we show the distribution of the measured line-of-sight velocities (given in the rest frame of the Earth) for all detected filaments, weighted by the intensity. We find the multimodal distribution to have two distinct pairs of symmetric peaks. We fit Gaussians to the peaks and find that the two dominant high-velocity peaks are centered around -778 and $+932 \text{ km s}^{-1}$, while the two narrower, lower-velocity features have fitted centers at -177 and $+303 \text{ km s}^{-1}$. Assuming symmetry along the line of sight, this allows the determination of the total radial velocity of the system. The mean of the Doppler velocities of the high-velocity blue- and redshifted features is 77 km s^{-1} , while for the low-velocity features is 63 km s^{-1} . We can therefore estimate the total system radial velocity as $v_{\text{sys}} = 70 \pm 7 \text{ km s}^{-1}$. Given the

observational epoch (2023 October 16), we compute the heliocentric correction using ASTROPY to be $v_{\text{H}} = 8.08 \text{ km s}^{-1}$. We thus find a total system line-of-sight velocity in the rest frame of the Sun to be $v_{\text{sys}} = 78 \pm 4 \text{ km s}^{-1}$.

From Equation (3), we can infer a deprojected, “true,” 3D separation of each filament from the central star d_{pro} , given by

$$d_{\text{pro}} = \sqrt{d_{\text{los}}^2 + r_{\text{sky}}^2}. \quad (6)$$

In turn, this yields a deprojected “true” velocity as

$$v_{\text{pro}} = \frac{d_{\text{pro}}}{\tau}. \quad (7)$$

In the lower panel of Figure 7, we show the distribution of all deprojected velocities. We find that the low-velocity features visible in the top panel disappear almost entirely as the deprojection pushes them to higher “true” velocities, because those filaments lay further away from the star, near the edge of the nebula. The redshifted low-velocity bump that remains corresponds to the small percentage (2.6%) of detected doublets that are due to contamination from a stationary sky line (see Section 3.3). We find that, given the small number of doublets in that region, and their generally small fluxes, these features have a negligible impact on the elliptical fit. We thus find strong evidence that the nebula is expanding with a mean velocity of $\approx 1000 \text{ km s}^{-1}$. The standard deviation of the Gaussians is 115 and 96 km s^{-1} for the blue and red components, respectively. As a measure of the range of velocities in the filaments, the vertical dashed lines in the bottom panel of Figure 7 indicate the 99% confidence interval on the filament velocities. We find the maximum red- and blueshifted velocities to be 1440 and 1380 km s^{-1} , respectively, while the minima are 650 and 510 km s^{-1} .

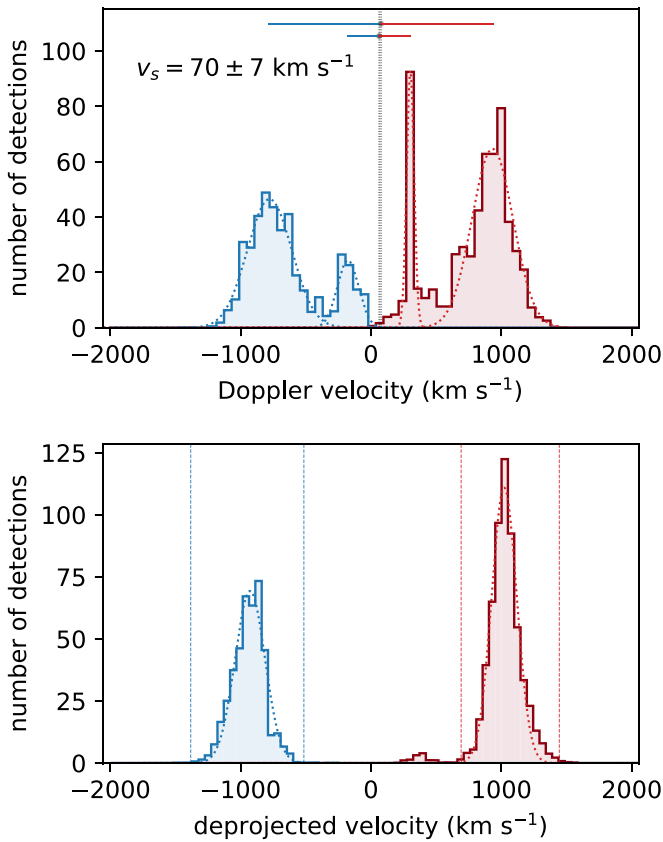


Figure 7. Top: histogram of the measured Doppler shift for all detected [S II] doublets, weighted by the measured flux in each doublet. The four peaks are fit with four Gaussians, finding two high-velocity broad peaks centered on -778 and $+932$ km s^{-1} , and two narrower, lower-velocity features centered on -177 and $+303$ km s^{-1} . The peak-to-peak distance between symmetric peaks is shown with the horizontal lines, while the vertical dashed line shows the mean velocity between each Gaussian pair. Assuming a spherically symmetric ejecta, this mean velocity provides an estimate of the total radial velocity of the system, which we find to be $v_s = 70 \pm 7$ km s^{-1} . In this figure, all velocities are given in the rest frame of Earth. The heliocentric correction is found to be $v_H = +8.08$ km s^{-1} , yielding a total system line-of-sight velocity in the rest frame of the Sun to be $v_{\text{sys}} = 78 \pm 4$ km s^{-1} . Bottom: velocity distribution for the deprojected velocities computed via Equations (2) and (7). The distribution becomes almost fully bimodal, with peaks at ± 1000 km s^{-1} . The fitted central velocities are $\bar{v}_b = -927 \pm 4$ and $\bar{v}_r = 1022 \pm 2$ km s^{-1} , for the blue and redshifted components, respectively. The vertical dashed lines indicate the 99% confidence interval on the filament velocities.

From both panels of Figure 7, we can clearly see that the size and intensity of redshifted filaments are higher than for blueshifted ones. By separately integrating the flux in all red- and blueshifted filaments, we find that there is 40% more flux measured in redshifted emission in the $\approx 10\%$ of the nebula covered by our KCWI-red observations. As the redshifted filaments lie farther away from us, this cannot be due to a selection effect and may hint at evidence of asymmetry in the ejecta. In their analysis of a single long-slit spectrum placed at a position angle 30° east of north and close to the central star, A. Ritter et al. (2021) found the opposite to be true, i.e., a higher flux in the blueshifted emission. Although the area covered by the long-slit spectrum is much smaller than the one covered by our IFU observations, the discrepancy might indicate that there is variation across the nebula on the plane of the sky. A wider coverage of the nebula is needed to confirm the possible asymmetry in the ejecta.

3.5. Comparison with Infrared Imaging

Based on the imaging from WISE, V. V. Gvaramadze et al. (2019) defined the edge of the bright inner infrared region to be $\approx 1'$. At the Gaia distance to this system, this corresponds to approximately 0.67 pc in radius. In our data set, we find that all of the filaments that appear close to the central star in the plane of the sky show high Doppler shifts, implying that their separation from the star is large along the line of sight. We therefore find a cavity in the center of the supernova remnant, which was already noted in R. A. Fesen et al. (2023), and a sharp inner edge to the filamentary structure. The location of this inner edge is consistent with the outer edge of the bright, inner infrared ring (see Figure 8).

In Figure 8 we show the WISE W4 image at $22 \mu\text{m}$. Following the methodology of V. V. Gvaramadze et al. (2019), we plot the WISE image at two different intensity scales. This allows us to highlight the edges of the bright inner region and the less bright outer nebula. In order to aid interpretation of the WISE W4 image, contours of constant flux are also shown in the figure using a global/continuous intensity scale. The 14 contours shown are separated in flux by $8 \mu\text{Jy}$, from the background level of 5.43 mJy. In order to make a comparison between the spatial position of the filaments detected in this work, and the infrared nebula, we plot the deprojected line-of-sight positions of all measured [S II] emission, using our best-fit value of $k = 0.97$. The deprojected line-of-sight positions are converted into an effective decl., which is equivalent to a rotation of 90° toward the viewer. The positions are also reflected from the left to the right of the central star (similar to Figure 6) in order to aide the comparison of the circular features. Assuming the nebula has a global spherical symmetry, this procedure allows us to compare the radial location of two key features: the narrow filaments and the infrared dusty nebula. We find strong evidence of a sharp, albeit jagged, boundary between the filaments and the bright, inner dust region. The filaments in Figure 8 are seen to cover the full radial extent of the outer nebula (dark purple region), where the gradient in infrared flux appears to be the strongest. The fact that the filaments do not reach the edge of the outer nebula along the x -axis (R.A.) is due to the footprint of the KCWI observations only extending out to the edge of the brightest [S II] filament, which reaches a maximum of $\text{R.A.} = 0^{\text{h}}53^{\text{m}}26^{\text{s}}$, and not beyond that (see Figure 1).

4. Summary

We have here presented a detailed description of the velocity structure in the supernova remnant Pa 30 as revealed by the analysis of the Doppler-shifted [S II] 6717/6731 \AA emission in the filaments of the nebula detected with KCWI-red. From our analysis, we can deduce that:

1. The age of the nebula is consistent with Pa 30 being the remnant of SN 1181. This is consistent with previous studies (A. Ritter et al. 2021; R. A. Fesen et al. 2023). Our 3D analysis allows us to confirm that the velocities in the spectra are almost ballistic, and we can therefore derive the time of the supernova explosion to be $t_0 = 1152^{+77}_{-75}$ yr.
2. The distribution of velocities in the ejecta is both narrow and highly symmetric. As we can see from Figure 7, the velocity distribution is tightly peaked at about 1000 km s^{-1} in both the blue- and redshifted material.

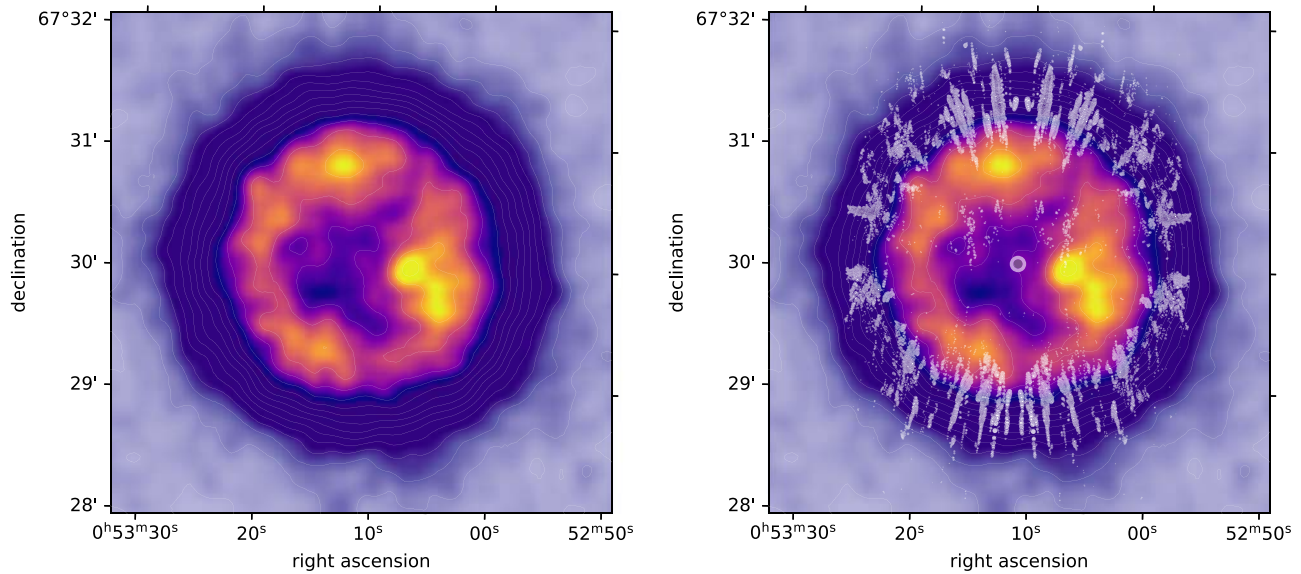


Figure 8. Left: WISE W4 (22 μm) image from the WISE image service (E. L. Wright et al. 2010). Because the inner infrared nebula in the WISE image is much brighter than the outer one, to show the location of both nebulae we superimpose two versions of the same image with different contrast levels, following the method of V. V. Gvaramadze et al. (2019), so that the outer nebula appears in uniform dark purple. For clarity, we also overlay contours of constant W4 infrared flux (thin white lines). The 14 contours plotted are evenly spaced in flux, with a separation of 8 μJy , from 5.44 to 5.54 mJy. The minimum and maximum flux in the image are 5.43 and 5.55 mJy, respectively. Right: the WISE image is the same as in the left plot. On top of the WISE image, we plot as white points the deprojected positions of the filaments using our best-fit value of the ballistic fraction, k . The deprojected positions have been reflected, as they are in Figure 6, and rotated by 90° toward the viewer, turning line-of-sight positions into sky positions, while preserving the angular size.

We find the maximum red- and blueshifted velocities, defined as the 99% confidence interval in the observed distribution, to be 1440 and 1380 km s^{-1} , respectively, while the minima are 650 and 510 km s^{-1} .

3. The ejecta show a strong asymmetry in flux along the line of sight, which may hint at an asymmetric explosion. The redshifted filaments are brighter and more numerous than the blueshifted ones, even if we would expect the opposite to be true due to selection effects. We find that the total flux from redshifted filaments is 40% higher than the flux from blueshifted ones. This is tantalizing evidence for asymmetry in the explosion; however, given the rather small area covered by our IFU observations, it may not be significant. Further IFU spectroscopic observations with wider coverage of the nebula will confirm if there exists a global asymmetry in the nebula ejecta, providing important constraints on dynamical models of the ejecta.
4. We confirm the presence of a large cavity in the remnant. All of the filaments that appear close to the central star in the plane of the sky show very high line-of-sight velocities, implying that their line-of-sight separation from the star is large. The presence of a cavity had previously been inferred from long-slit spectroscopic observations (R. A. Fesen et al. 2023). The KCWI observations presented here have allowed the detection of a sharp inner edge to the filamentary emission in the ejecta that coincides with the outer edge of the bright ring detected in the infrared. Adopting the Gaia distance of 2.3 kpc, we measure the inner and outer radius of the filamentary shell to be $r_{\text{in}} \approx 0.6$ pc and $r_{\text{out}} \approx 1.0$ pc, respectively. The edge of this inner infrared ring has previously been interpreted to be indicative of the position of the reverse shock, as in the shocked region the dust grains should have been sublimated and destroyed (T. Ko et al. 2024; P. C. Duffell et al. 2024).

5. The velocities in the filaments are consistent with being ballistic. We estimate the ballistic fraction in the ejecta velocities to be $k = 0.97^{+0.09}_{-0.08}$. With k very close to unity, there is no significant evidence that deceleration or acceleration has occurred in the ejecta. If the observed edge between the infrared cavity and the filaments indicates the location of the reverse shock, then we expect a large fraction of the ejecta to have been shocked already; the low deceleration observed would still be consistent with this scenario, and it would indicate a low density in the CSM. In the model by P. C. Duffell et al. (2024), for example, the deceleration induced by the reverse shock leads to a ballistic fraction of 0.93, consistent with our measurement.

Acknowledgments

We thank Rob Fesen for providing the [S II] narrowband imaging and providing helpful comments on the Letter. We also thank Eliot Quatterl for the helpful discussions. T.C. was supported by NASA through the NASA Hubble Fellowship grant HST-HF2-51527.001-A awarded by the Space Telescope Science Institute, which is operated by the Association of Universities for Research in Astronomy, Inc., for NASA, under contract NAS5-26555. I.C. was also supported by NASA through grants from the Space Telescope Science Institute, under NASA contracts NASA.22K1813, NAS5-26555, and NAS5-03127. This research was supported in part by grant NSF PHY-1748958 to the Kavli Institute for Theoretical Physics (KITP). O.T. was supported by FONDECYT grant 11241186.

This publication makes use of data products from the Wide-field Infrared Survey Explorer, which is a joint project of the University of California, Los Angeles, and the Jet Propulsion Laboratory/California Institute of Technology, funded by the National Aeronautics and Space Administration.

This research made use of Montage. It is funded by the National Science Foundation under grant No. ACI-1440620, and was previously funded by the National Aeronautics and Space Administration’s Earth Science Technology Office, Computation Technologies Project, under Cooperative Agreement Number NCC5-626 between NASA and the California Institute of Technology.

Facility: Keck:II (KCWI).

Software: ASTROPY (Astropy Collaboration et al. 2013, 2018), SCIPY (P. Virtanen et al. 2020), QFITSVIEW (T. Ott 2012), MONTAGE (J. C. Jacob et al. 2010).

Appendix A

Details on Data Reduction and Methodology

We reduced the raw KCWI data using the official PYTHON KCWI Data Reduction Pipeline¹⁴ (DRP; D. Neill et al. 2023). The DRP reads in afternoon calibration frames, science exposures, and standard star observations to produce flux-calibrated 3D data cubes of the science targets. The default parameters use ThAr arc spectra to construct a wavelength solution along with a master flat field derived from an average stack of internally illuminated flats.

In general, a raw science exposure is bias subtracted and gain corrected; cosmic rays are flagged and removed; the wavelength solution derived from calibration frames is applied; the frame is flat fielded; and a 1D sky model to the sky pixels in the spectra is subtracted from the data. At this point, the 2D data in detector coordinates is transformed into a 3D data cube, DAR corrected, and flux calibrated using the standard star observation.

















Although observations from both the blue and red channels undergo the same broad reduction steps, as mentioned above, cosmic-ray hits are significantly more pernicious on the red detector. While ASTROCRAPPY (C. McCully et al. 2018; P. G. van Dokkum 2001) is largely effective for the blue channel “hot-pixel”-type cosmic rays, the red channel features a much more diverse array of cosmic ray morphologies that current automated routines are unequipped to handle. Instead, we opt to take several exposures and use their median to make cosmic-ray masks for each constituent exposure.

In practice, given three exposures of the same target under the same conditions, we construct a median exposure that effectively removes the cosmic rays and leaves just the science target. For each constituent exposure, we subtract off the median science frame we just constructed; the difference image then contains only cosmic rays plus some noise. We apply sigma-clipping to the difference image and convert the clipped pixels into a binary cosmic-ray mask. We then run a customized version of the KCWI DRP¹⁵ that reads in these cosmic-ray masks, flags the affected regions, and excludes such pixels from the final science outputs.

KCWI DRP processed cubes are stacked and mosaicked using KCWIKIT¹⁶ (N. Z. Prusinski & Y. Chen 2024). The full implementation is described in Y. Chen et al. (2021), but briefly, the individual science cubes are drizzled onto a common spatial grid with $0.''3 \times 0.''3$ sampling using the MONTAGE (J. C. Jacob et al. 2010) package. Each frame is also World Coordinate System corrected using an external narrow-band image.

To extract the Doppler information from the [S II] doublet in the mosaicked KCWI-red data, we create a mask to select only the brightest filaments (see Figure 1). The regions in the mask are determined by taking the mean flux average over the full data cube along the spectral dimension, between $\lambda = 6800$ and 6750 \AA , and subtracting the mean local continuum. This allows us to make a high-contrast image focused on all pixels with significant [S II] emission (lower panel of Figure 1). The wavelength range was chosen to include the minimally and maximally Doppler shifted doublets, with wavelength limits determined from visual inspection using the QFITSVIEW software (T. Ott 2012). This high-contrast image was subsequently turned into an initial binary mask by selecting the brightest 30% of pixels, after the exclusion of two bright and saturated stars (one being the central remnant, the other being located at R.A. = $0^{\text{h}}53^{\text{m}}19^{\text{s}}$ and decl. = $67^{\circ}29'50''$). This corresponds to a cut on mean fluxes less than $\langle F_{[\text{S II}]} \rangle < 0.001 \times 10^{-8} \text{ erg s}^{-1} \text{ cm}^{-3} \text{ arcsec}^{-2}$. This flux limit is about 4% of the maximum flux in the high-contrast image. After the masking of the two saturated stars, the spectral cube contained 25,580 spatial pixels within the observed footprint. The flux cut on the high-contrast image yielded 8084 spatial pixels selected for analysis. We only analyze pixels centered on a 3×3 pixel window, which is fully contained within the selected regions. This was done in order to further reduce contamination from noise, and ensure a homogeneous analysis across the full cube. This reduced the total number of analyzed spatial pixels from 8084 to 5575. The number of pixels that received a single, double, triple, and quadruple doublet fit are 2681, 2469, 416, and 9, respectively. This yielded a total number of 8903 fitted [S II] doublets.

ORCID iDs

Tim Cunningham  <https://orcid.org/0000-0001-7296-3533>
 Ilaria Caiazzo  <https://orcid.org/0000-0002-4770-5388>
 Nikolaus Z. Prusinski  <https://orcid.org/0000-0001-5847-7934>
 James Fuller  <https://orcid.org/0000-0002-4544-0750>
 John C. Raymond  <https://orcid.org/0000-0002-7868-1622>
 S. R. Kulkarni  <https://orcid.org/0000-0001-5390-8563>
 James D. Neill  <https://orcid.org/0000-0002-0466-1119>
 Paul Duffell  <https://orcid.org/0000-0001-7626-9629>
 Chris Martin  <https://orcid.org/0000-0002-8650-1644>
 Odette Toloza  <https://orcid.org/0000-0002-2398-719X>
 David Charbonneau  <https://orcid.org/0000-0002-9003-484X>
 Scott J. Kenyon  <https://orcid.org/0000-0003-0214-609X>
 Mateusz Matuszewski  <https://orcid.org/0000-0003-2821-1750>
 Rosalie McGurk  <https://orcid.org/0000-0003-2064-4105>
 Abigail Polin  <https://orcid.org/0000-0002-1633-6495>
 Philippe Z. Yao  <https://orcid.org/0000-0003-3024-7218>

References

- Astropy Collaboration, Price-Whelan, A. M., Sipőcz, B. M., et al. 2018, *AJ*, **156**, 123
- Astropy Collaboration, Robitaille, T. P., Tollerud, E., et al. 2013, *A&A*, **558**, A33
- Bailer-Jones, C. A. L., Rybizki, J., Fouesneau, M., Demleitner, M., & Andrae, R. 2021, *AJ*, **161**, 147
- Chen, Y., Steidel, C. C., Erb, D. K., et al. 2021, *MNRAS*, **508**, 19

¹⁴ https://github.com/Keck-DataReductionPipelines/KCWI_DRP

¹⁵ https://github.com/prusinski/KCWI_DRP

¹⁶ <https://github.com/yuguangchen1/KcwiKit>

- Cutri, R. M., Wright, E. L., Conrow, T., et al. 2012, *yCat*, **2311**, 0, VizieR Online Data Catalog: WISE All-Sky Data Release (+ 2012), VizieR On-line Data Catalog: II/311
- Del Zanna, G., Dere, K. P., Young, P. R., Landi, E., & Mason, H. E. 2015, *A&A*, **582**, A56
- Duffell, P. C., Polin, A., & Mandal, S. 2024, arXiv:2403.13641
- Fasano, G., & Franceschini, A. 1987, *MNRAS*, **225**, 155
- Fesen, R. A., Schaefer, B. E., & Patchick, D. 2023, *ApJL*, **945**, L4
- Foley, R. J., Challis, P. J., Chornock, R., et al. 2013, *ApJ*, **767**, 57
- Gvaramadze, V. V., Gräfener, G., Langer, N., et al. 2019, *Natur*, **569**, 684
- Jacob, J. C., Katz, D. S., Berriman, G. B., et al., 2010 Montage: An Astronomical Image Mosaicking Toolkit, Astrophysics Source Code Library, ascl:1010.036
- Jansen, F., Lumb, D., Altieri, B., et al. 2001, *A&A*, **365**, L1
- Ko, T., Suzuki, H., Kashiyama, K., et al. 2024, *ApJ*, **969**, 116
- Lykou, F., Parker, Q. A., Ritter, A., et al. 2023, *ApJ*, **944**, 120
- McCully, C., Crawford, S., Kovacs, G., et al. 2018, *astropy/astrocrappy*: v1.0.5 Zenodo Release, v1.0.5, Zenodo, doi:10.5281/zenodo.1482019
- Morrissey, P., Matuszewski, M., Martin, D. C., et al. 2018, *ApJ*, **864**, 93
- Neill, D., Matuszewski, M., Martin, C., Brodheim, M., & Rizzi, L., 2023 KCWI_DRP: Keck Cosmic Web Imager Data Reduction Pipeline in Python, Astrophysics Source Code Library, ascl:2301.019
- O'Dell, C. R., & Handron, K. D. 1996, *AJ*, **111**, 1630
- Oskinova, L. M., Gvaramadze, V. V., Gräfener, G., Langer, N., & Todt, H. 2020, *A&A*, **644**, L8
- Ott, T., 2012 QFitsView: FITS file viewer, Astrophysics Source Code Library, ascl:1210.019
- Parker, Q. A., Bojčić, I. S., & Frew, D. J. 2016, *JPhCS*, **728**, 032008
- Peacock, J. A. 1983, *MNRAS*, **202**, 615
- Prusinski, N. Z., & Chen, Y., 2024 KCWIKit: KCWI Post-Processing and Improvements, Astrophysics Source Code Library, ascl:2404.003
- Ritter, A., Parker, Q. A., Lykou, F., et al. 2021, *ApJL*, **918**, L33
- Schaefer, B. E. 2023, *MNRAS*, **523**, 3885
- Schwab, J. 2021, *ApJ*, **906**, 53
- Seok, J. Y., Koo, B.-C., Zhao, G., & Raymond, J. C. 2020, *ApJ*, **893**, 79
- Shara, M. M., Zurek, D., De Marco, O., et al. 2012, *AJ*, **143**, 143
- van Dokkum, P. G. 2001, *PASP*, **113**, 1420
- Vaytet, N. M. H., O'Brien, T. J., & Rushton, A. P. 2007, *MNRAS*, **380**, 175
- Virtanen, P., Gommers, R., Oliphant, T. E., et al. 2020, *NatMe*, **17**, 261
- Weisskopf, M. C., Tananbaum, H. D., Van Speybroeck, L. P., & O'Dell, S. L. 2000, *Proc. SPIE*, **4012**, 2
- Wesson, R., Matsuura, M., Zijlstra, A. A., et al. 2024, *MNRAS*, **528**, 3392
- Wright, E. L., Eisenhardt, P. R. M., Mainzer, A. K., et al. 2010, *AJ*, **140**, 1868
- Yao, P. Z., Quataert, E., & Goulding, A. 2023, *MNRAS*, **524**, 1031
- Zhong, Y., Kashiyama, K., Takasao, S., Shigeyama, T., & Fujisawa, K. 2024, *ApJ*, **963**, 26